DIRECTION-DEPENDENT RECEPTANCES FOR ANISOTROPIC NICKEL SUPERALLOY

Andrew Honeycutt[1], Mike Glavicic[2], and Tony L. Schmitz[1]
[1]Department of Mechanical Engineering and Engineering Science
University of North Carolina at Charlotte, Charlotte, NC
[2]Rolls Royce Corporation, Indianapolis, IN

INTRODUCTION

It is common practice to produce monolithic metallic components with thin ribs from solid billets by machining. This enables complex parts with high strength-to-weight ratio to be produced without significant assembly time and cost. For high material cost situations, it is often preferred to apply near net shape strategies, where an initially thin feature (produced by forging or additive processes, for example) is machined to produce a thinner feature with the required dimensions and surface integrity. Application domains range from aerospace components to laptop cases.

A significant challenge in near net shape applications is that the low dynamic stiffness of the thin rib features limits both machining stability (i.e., chatter can occur) and part accuracy (via the surface location errors that can arise from forced vibrations) [1]. If the dynamic response of the workpiece is modeled, however, machining parameters and tool paths can be selected to produce acceptable parts. This process is complicated when machining anisotropic materials. In this case, the dynamics are direction-dependent due to the variation in elastic modulus with crystal orientation.

In this research, the single crystal superalloy CMSX-4 was selected for machining trials and dynamics prediction. This alloy was developed for gas turbine engine airfoil, seal, and combustor components to provide high temperature creep strength, fatigue resistance, oxidation resistance, and performance retention in thin-walled configurations. Its nominal composition is provided in Table 1 [2].

Table 1. CMSX-4 nominal composition.

Element	Wt.%	Element	Wt.%
Cr	6.5	Al	5.6
Co	9.6	Ti	1.0
W	6.4	Ta	6.5
Re	3.0	Hf	0.1
Mo	0.6	Ni	Balance

An analytical approach is presented here to describe the natural frequency of fixed-free beams, as well as the change in natural frequency as material is removed by milling. Fixed-free beams with stepped profiles are used to represent the thin ribs geometries and subsequent material removal. Due to the CMSX-4 anisotropy, results are presented for two material directions with corresponding differences in elastic modulus.

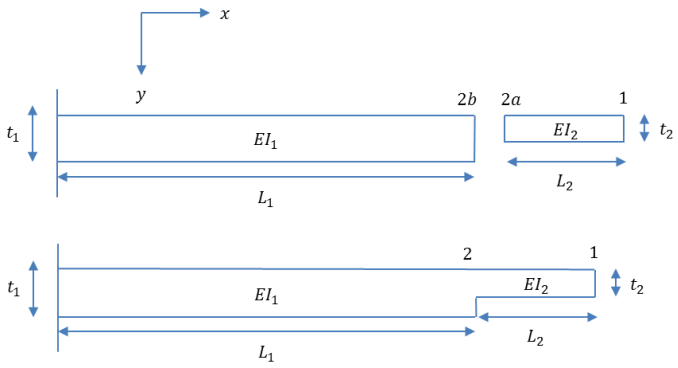

Figure 1. Beam model for RCSA. (Top) The two components and associated coordinates (1 and $2a$ for the free-free component and $2b$ for the fixed-free component) are identified. (Bottom) The assembly and associated coordinates (1 and 2) are shown.

ANALYTICAL MODEL

Receptance coupling substructure analysis (RCSA) is a frequency domain, analytical procedure used to couple component receptances (or frequency response functions) in order to predict the assembly receptances [3-4]. In this work, the free-free receptances for the machined section of a beam were rigidly coupled to the remaining (unmachined) fixed-free section; see Fig. 1. Using rigid compatibility and equilibrium conditions, the assembly direct receptances, $H_{11} = \frac{Y_1}{F_1}$ and $H_{22} = \frac{Y_2}{F_2}$, at assembly coordinates Y_1 and Y_2 are written as a function of the component receptances at coordinates 1, $2a$, and $2b$; see [3] for the derivation. The required direct and cross receptances for the free-free (coordinates 1 and $2a$) and fixed-free (coordinate $2b$) components are:

- $h_{11} = \frac{y_1}{f_1}$, $h_{12a} = \frac{y_1}{f_{2a}}$, $h_{2a1} = \frac{y_{2a}}{f_1}$, $h_{2a2a} = \frac{y_{2a}}{f_{2a}}$, and $h_{2b2b} = \frac{y_{2b}}{f_{2b}}$, where y_i is the component

displacement and f_j is the (internal) component force

- $l_{11} = \frac{y_1}{m_1}$, $l_{12a} = \frac{y_1}{m_{2a}}$, $l_{2a1} = \frac{y_{2a}}{m_1}$, $l_{2a2a} = \frac{y_{2a}}{m_{2a}}$, and $l_{2b2b} = \frac{y_{2b}}{m_{2b}}$, where m_j is the (internal) component moment
- $n_{11} = \frac{\theta_1}{f_1}$, $n_{12a} = \frac{\theta_1}{f_{2a}}$, $n_{2a1} = \frac{\theta_{2a}}{f_1}$, $n_{2a2a} = \frac{\theta_{2a}}{f_{2a}}$, and $n_{2b2b} = \frac{\theta_{2b}}{f_{2b}}$, where θ_i is the component rotation
- $p_{11} = \frac{\theta_1}{m_1}$, $p_{12a} = \frac{\theta_1}{m_{2a}}$, $p_{2a1} = \frac{\theta_{2a}}{m_1}$, $h_{2a2a} = \frac{\theta_{2a}}{m_{2a}}$, and $p_{2b2b} = \frac{\theta_{2b}}{m_{2b}}$.

The assembly receptances are provided in Eqs. 1 and 2 [3].

$$\begin{bmatrix} H_{11} & L_{11} \\ N_{11} & P_{11} \end{bmatrix} = \begin{bmatrix} h_{11} & l_{11} \\ n_{11} & p_{11} \end{bmatrix} - \begin{bmatrix} h_{12a} & l_{12a} \\ n_{12a} & p_{12a} \end{bmatrix} \left(\begin{bmatrix} h_{2a2a} & l_{2a2a} \\ n_{2a2a} & p_{2a2a} \end{bmatrix} + \begin{bmatrix} h_{2b2b} & l_{2b2b} \\ n_{2b2b} & p_{2b2b} \end{bmatrix} \right)^{-1} \begin{bmatrix} h_{2a1} & l_{2a1} \\ n_{2a1} & p_{2a1} \end{bmatrix} \quad (1)$$

$$\begin{bmatrix} H_{22} & L_{22} \\ N_{22} & P_{22} \end{bmatrix} = \begin{bmatrix} h_{2a2a} & l_{2a2a} \\ n_{2a2a} & p_{2a2a} \end{bmatrix} - \begin{bmatrix} h_{2a2a} & l_{2a2a} \\ n_{2a2a} & p_{2a2a} \end{bmatrix} \left(\begin{bmatrix} h_{2a2a} & l_{2a2a} \\ n_{2a2a} & p_{2a2a} \end{bmatrix} + \begin{bmatrix} h_{2b2b} & l_{2b2b} \\ n_{2b2b} & p_{2b2b} \end{bmatrix} \right)^{-1} \begin{bmatrix} h_{2a2a} & l_{2a2a} \\ n_{2a2a} & p_{2a2a} \end{bmatrix} \quad (2)$$

The component receptances can be obtained from measurements or models. In this work, the Timoshenko beam model was implemented to find the free-free receptances. This requires a numerical solution of the partial differential equation displayed in Eq. 3 [5-6], where E is the elastic modulus, I is the second moment of area, ρ is the density, A is the cross-sectional area, G is the shear modulus, and $\hat{k}$ is a shape factor that depends on the beam's cross section [7].

To determine the required fixed-free ($2b2b$) receptances for the L_1 section component, the free-free receptances for this component (obtained from Eq. 3) were rigidly coupled to a rigid boundary (i.e., zero receptances). Equation 1 was also applied for this sub-step, where the $2b$ coordinate was assigned to the rigid boundary and the 1 and $2a$ coordinates to the L_1 section component. The RCSA method reported here builds on prior finite element-based models used to predict the thin rib dynamics and, in many cases, the change in the rib dynamics as material is removed [8-26].

$$\left(\frac{\partial^2 y}{\partial t^2} + \frac{EI}{\rho A}\frac{\partial^4 y}{\partial x^4}\right) + \left(\frac{\rho I}{\hat{k}AG}\frac{\partial^4 y}{\partial t^4} + \frac{EI}{\hat{k}AG}\frac{\partial^4 y}{\partial x^2 \partial t^2}\right) - \left(\frac{I}{A}\frac{\partial^4 y}{\partial x^2 \partial t^2}\right) = 0 \quad (3)$$

EXPERIMENTAL RESULTS

The test sample geometry shown in Fig. 2 was sectioned from cast CMSX-4 76×152×12 mm plates using wire EDM. The solidification <001> direction for the plates was nominally along the 152 mm dimension. This is the direction of lowest modulus. Two orientations within the cast plate were selected to interrogate the effect of modulus on the sample receptances. The orientations are displayed in Fig. 3. The 0 deg samples were collected from one plate and the 90 deg samples from a second plate. These samples were then finish machined as shown in Fig. 1 to measure the change in fixed-free natural frequency as material was removed. The measured natural frequency variation was then compared to RCSA predictions.

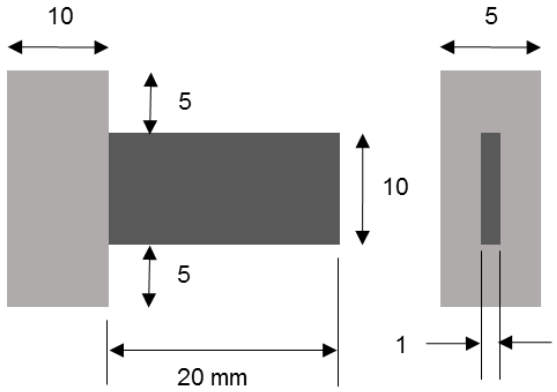

Figure 2. Sample geometry.

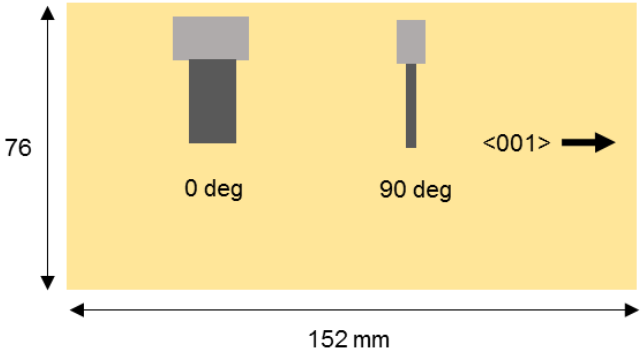

Figure 3. Sample orientations within the cast CMSX-4 plates.

The sample densities and elastic moduli were measured to obtain the values required for the RCSA analyses. Archimedes' water displacement method

was used to determine the density. The following steps were completed.

- A container of water was placed on a scale and the mass was recorded.
- The sample was submerged in the water with a thin wire so that it was fully submerged, but not touching the bottom of the container.
- The mass was again recorded.
- Since the buoyant force is equal to the weight of the displaced water, the volume of the sampled was estimated using the measured force and water density.
- The sample mass was measured.
- The density was calculated using the sample mass and volume.

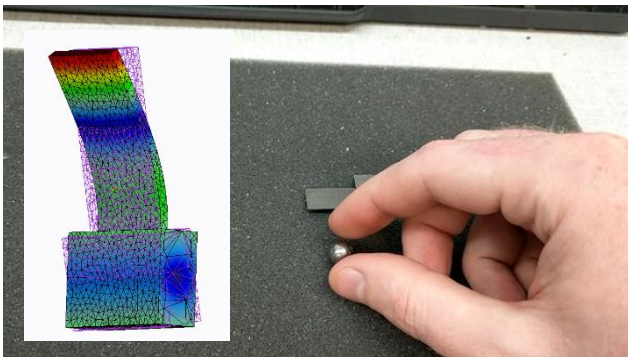

Figure 4. Elastic modulus determination. The free-free boundary condition impact testing setup and finite element model (inset) are shown.

The elastic modulus was measured by free-free boundary condition impact testing. The samples were placed on a soft foam foundation and excited by dropping a steel sphere at the top free edge of the thin rib. The corresponding sound signal was measured and converted to the frequency domain to determine the fundamental natural frequency. A finite element model of the sample (with free-free boundary conditions) was then generated and the elastic modulus was varied until the fundamental natural frequency matched the measured value; the measured density values were used as input to the finite element model. See Fig. 4 for the setup. The density and modulus measurement were repeated for both sample directions from Fig. 3 (0 deg and 90 deg). The results are provided in Table 2.

Table 2. Measured sample density and modulus.

Orientation	Density (kg/m^3)	Elastic modulus (GPa)
0 deg	8797	188
90 deg	8695	166

Receptance measurements were completed using a modal hammer (PCB 086C04) to excite the beam and a laser vibrometer (Polytec OFV 5000 controller/OFV 534 laser head) to measure the velocity; see Fig. 5, which shows the sample clamped in a vise to approximate fixed-free boundary conditions.

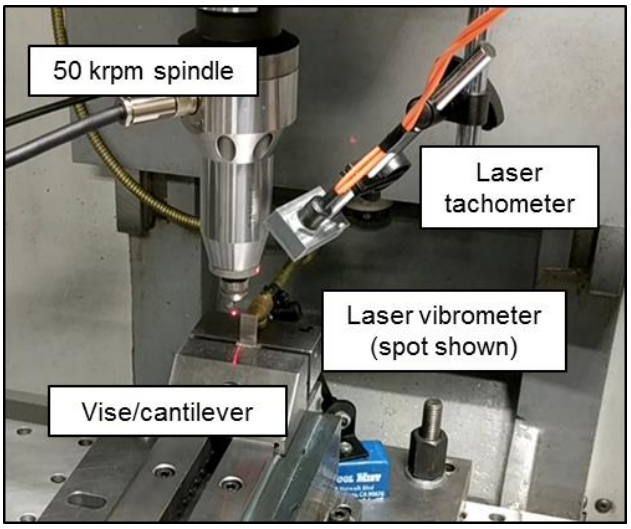

Figure 5. Experimental setup. The rib was machined to reduce the thickness and the receptance was measured for multiple L_2 values.

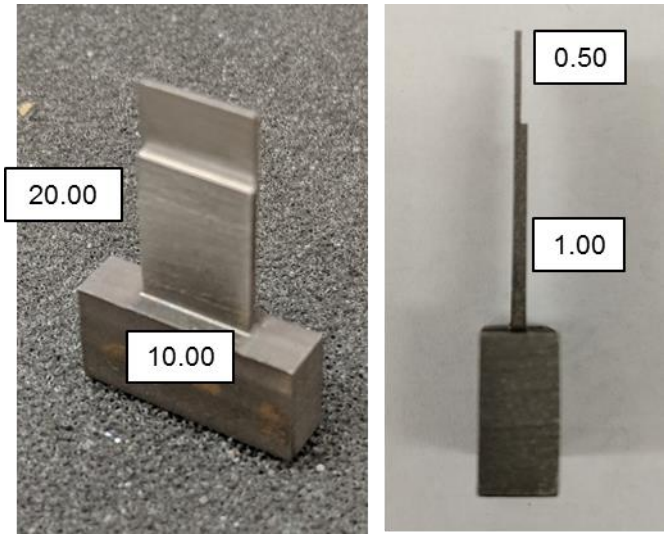

Figure 6. Photograph of machined sample (dimensions in mm).

Direct receptance measurements were performed at the sample's free end. The length of the reduced thickness section, L_2, was changed by machining, where a 1.50 mm diameter two-flute solid carbide endmill (approximately 10 mm stickout length) was

used (0.010 mm/tooth, 11000 rpm). The cutting flutes were ground away above the selected axial depth to avoid contact between the vibrating tool and machined surface. The beam thickness was reduced from 1 mm (t_1 from Fig. 1) to 0.5 mm (t_2) in 0.025 mm axial steps with a radial depth of 0.50 mm. Measurements were performed after the desired reduced thickness length was obtained. A photograph of a machined sample is displayed in Fig. 6.

The variation in natural frequency, f_n, with L_2 is provided in Table 3 for the two sample orientations. Note that the natural frequencies differ; the higher values are associated with the 0 deg sample that had the higher modulus in the flexible bending direction.

Table 3. Variation in measured natural frequencies with L_2 for both sample orientations.

0 deg		90 deg	
L_2 (mm)	f_n (Hz)	L_2 (mm)	f_n (Hz)
0	1874	0	1777
1.27	1970	1.27	1879
2.54	2074	2.54	1989
3.81	2163	3.81	2109
5.08	2240	5.08	2114
6.35	2296	6.35	2289

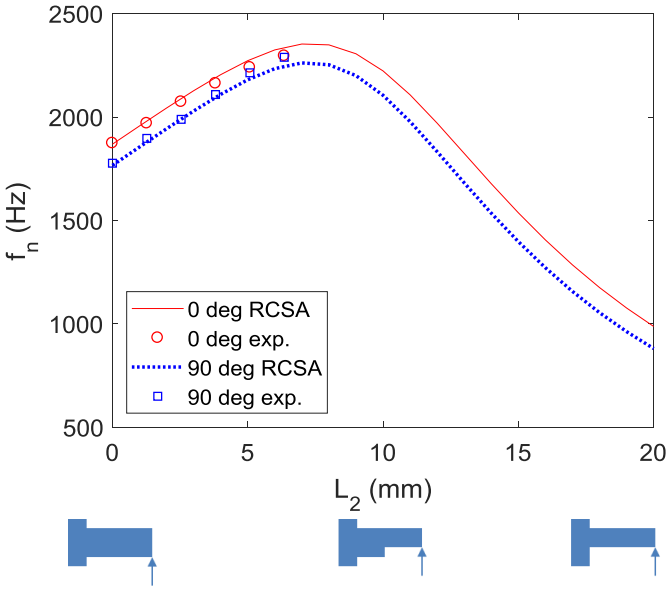

Figure 7. Comparison of measured and predicted natural frequencies. The variation in natural frequencies with L_2 is provided for both sample orientations.

A comparison between measured natural frequencies and RCSA predictions is displayed in Fig. 7, where the RCSA natural frequencies were identified from the predicted receptances using peak-picking [3]. An interesting trend is revealed by the simulation. It is observed that the natural frequencies first increase and then decrease as additional material is removed. The initial increase is obtained due to the mass removal without significant change in the fixed-free beam stiffness. With additional material removal, however, the beam stiffness decreases dramatically and the natural frequency decreases despite further mass removal.

CONCLUSIONS

An analytical approach was presented for predicting thin rib, fixed-free beam dynamics with varying geometries. The method was based on receptance coupling substructure analysis (RCSA). The effect of workpiece material anisotropy on receptance was investigated by choosing two different sample orientations within two CMSX-4 nickel superalloy plates. Separate free-free impact testing measurements verified the difference in elastic moduli between the two directions.

The outcome of both predictions and experiments was that the receptances differed between the two orientations (0 deg – flexible bending direction perpendicular to the solidification direction and 90 deg – parallel). The implications for machining are that the operating parameters may need to be changed depending on the orientation of the rib's flexible direction. For example, the preferred spindle speed to avoid chatter for one direction may be different than another. The best speeds for chatter avoidance are proportional to the natural frequency [1]. If the natural frequencies differ, then a stable speed for one orientation may be unstable for another. Given the RCSA model, however, the receptances can be predicted and optimal machining parameters may be selected in a pre-process manner.

ACKNOWLEDGEMENTS

The authors gratefully acknowledge financial support from MAI BA-21 (USAF contract number FA8650-17-2-5246).

REFERENCES

[1] Schmitz, T. and Smith, K.S., 2009, Machining Dynamics: Frequency Response to Improved Productivity, Springer, New York, NY.

[2] Harris, K. and Wahl, J.B., 2004, Improved single crystal superalloys CMSX-4 (SLS) [La+Y] and CMSX-486, Superalloys 2004, K.A. Green, T.M. Pollock, and H. Harada, Eds., TMS (The Minerals, Metals & Materials Society).

[3] Schmitz, T. and Smith, K.S., 2012, Mechanical Vibrations: Modeling and Measurement, Springer, New York, NY.
[4] Bishop, R.E.D., and Johnson, D.C., 1960, The Mechanics of Vibration, Cambridge University Press, Cambridge, UK.
[5] Weaver, Jr., W., Timoshenko, P., and Young, D., 1990, Vibration Problems in Engineering, 5th Ed., John Wiley and Sons, New York, NY.
[6] Schmitz, T. and Duncan, G.S., 2005, Three-component receptance coupling substructure analysis for tool point dynamics prediction, Journal of Manufacturing Science and Engineering, 127/4: 781-790.
[7] Hutchinson, J., 2001, Shear coefficients for Timoshenko beam theory, Journal of Applied Mechanics, 68: 87-92.
[8] Budak, E., Altintas, Y., 1995, Modeling and avoidance of static form errors in peripheral milling of plates, International Journal of Machine Tools & Manufacture, 35: 459-476.
[9] Tlusty, J., Smith, S., and Winfough, W., 1996, Techniques for the use of long slender end mills in high-speed milling, Annals of the CIRP, 45/1: 393-396.
[10] Smith, S. and Dvorak, D., 1998, Tool path strategies for high speed milling aluminum workpieces with thin webs, Mechatronics, 8: 291-300.
[11] Ning, H., Zhigang, W., Chengyu, J., and Bing, Z., 2003, Finite element method analysis and control stratagem for machining deformation of thin-walled components, Journal of Materials Processing Technology, 139: 332-336.
[12] Ratchev, S., Nikov, S., and Moualek, I., 2004, Material removal simulation of peripheral milling of thin wall low-rigidity structures using FEA, Advances in Engineering Software, 35: 481-491.
[13] Ratchev, S., Liu, S., Huang, W., and Becker, A.A., 2004, Milling error prediction and compensation in machining of low-rigidity parts, International Journal of Machine Tools & Manufacture, 44: 1629-1641.
[14] Bravo, U., Altuzarra, O., López de Lacalle, L.N., Sánchez, J.A., and Campa, F.J., 2005, Stability limits of milling considering the flexibility of the workpiece and the machine, International Journal of Machine Tools & Manufacture, 45: 1669-1680.
[15] Ratchev, S., Liu, S., and Becker, A.A., 2005, Error compensation strategy in milling flexible thin-wall parts, Journal of Materials Processing Technology, 162-163: 673-681.
[16] Thevenot, V., Arnaud, L., Dessein, G., and Cazenave-Larroche, G., 2006, Influence of material removal on the dynamic behavior of thin-walled structures in peripheral milling, Machining Science and Technology, 10/3: 275-287.
[17] Mañé, I., Gagnol, V., Bouzgarrou, B.C., and Ray, P., 2008, Stability-based spindle speed control during flexible workpiece high-speed milling, International Journal of Machine Tools & Manufacture, 48: 184-194.
[18] Rai, J.K. and Xirouchakis, P., 2008, Finite element method based machining simulation environment for analyzing part errors induced during milling of thin-walled components, International Journal of Machine Tools & Manufacture, 48: 629-643.
[19] Seguy, S., Dessein, G., and Arnaud, L., 2008, Surface roughness variation of thin wall milling, related to modal interactions, International Journal of Machine Tools & Manufacture, 48: 261-274.
[20] Adetoro, O.B., Wen, P.H., Sim, W.M., and Vepa, R., 2009, Stability lobes prediction in thin wall machining, Proceedings of the World Congress on Engineering 2009 Vol I, WCE 2009, July 1-3, 2009, London, UK.
[21] Chen, W., Xue, J., Tang, D., Chen, H., and Qu, S., 2009, Deformation prediction and error compensation in multilayer milling processes for thin-walled parts, International Journal of Machine Tools & Manufacture, 49: 859-864.
[22] Gang, L., 2009, Journal of Materials Processing Technology, Study on deformation of titanium thin-walled part in milling process, 209: 2788-2793.
[23] Arnaud, L., Gonzalo, O., Seguy, S., Jauregi, H., and Peigné, G., 2011, Simulation of low rigidity part machining applied to thin-walled structures, International Journal of Advanced Manufacturing Technology, 54: 479-488.
[24] Izamshah, R., Mo, J.P.T, and Ding, S., 2011, Hybrid deflection prediction on machining thin-wall monolithic aerospace components, Proc. IMechE Part B: Journal of Engineering Manufacture, 226: 592-605.
[25] Smith, S., Wilhelm, R., Dutterer, B., Cherukuri, H., and Goel, G., 2012, Sacrificial structure preforms for thin part machining, CIRP Annals - Manufacturing Technology, 61: 379-382.
[26] Polishetty, A., Goldberg, M., Littlefair, G., Puttaraju, M., and Patil, P., 2014, A preliminary assessment of machinability of titanium allow Ti 6Al 4V during thin wall machining using trochoidal milling, Procedia Engineering, 97: 357-364.